INCLUSIVE PUBLISHING
TRUSTED SCIENCE

PAPER • OPEN ACCESS

Maximum likelihood bolometry for ASDEX upgrade experiments

View the article online for updates and enhancements.

Physica Scripta

PAPER

Maximum likelihood bolometry for ASDEX upgrade experiments

Teddy Craciunescu[1] , Emmanuele Peluso[2,*] , Andrea Murari[3,4] , Matthias Bernert[5] , Michela Gelfusa[2] , Riccardo Rossi[2], Luca Spolladore[2], Ivan Wyss[2], Pierre David[5] , Stuart Henderson[6] , Olivier Fevrier[7] , ASDEX Upgrade Team[8]

1   National Institute for Laser, Plasma and Radiation Physics, Magurele-Bucharest, Romania
2   University of Rome 'Tor Vergata', Roma, Italy
3   Consorzio RFX (CNR, ENEA, INFN, Universita' di Padova, Acciaierie Venete SpA), Padova, Italy
4   Istituto per la Scienza e la Tecnologia dei Plasmi, CNR, Padova, Italy
5   Max Planck Institute for Plasma Physics, 85748 Garching, Germany
6   CCFE,Culham Science Centre, Abingdon OX14 3DB, United Kingdom
7   École Polytechnique Fédérale de Lausanne (EPFL), Swiss Plasma Center (SPC), CH-1015 Lausanne, Switzerland
8   See author list of U. Stroth *et al* 2022 Nucl. Fusion 62 042006
*   Author to whom any correspondence should be addressed.

E-mail: emmanuele.peluso@uniroma2.it

Abstract

Bolometry is an essential diagnostic for calculating the power balances and for the understanding of different physical aspects of tokamak experiments. The reconstruction method based on the Maximum Likelihood (ML) principle, developed initially for JET, has been implemented for ASDEX Upgrade. Due to the availability of a limited number of views, the reconstruction problem is mathematically ill-posed. A regularizing procedure, based on the assumption of smoothness along the magnetic surfaces, given by plasma equilibrium, must also be implemented. A new anisotropic smoothing technique, which acts along locally oriented kernels, has been implemented. The performances of the method have been evaluated, in terms of shapes, resolution and of the derived radiated power, and compared with the bolometry method used routinely on ASDEX Upgrade. The specific advantage of the ML reconstruction algorithm consists of the possibility to assess the uncertainties of the reconstruction and to derive confidence intervals in the emitted radiation levels. The importance of this capability is illustrated.

1. Introduction

The total emission of radiation is a very important quantity for evaluating tokamak power balances and for understanding various physical processes [1]. The radiation patterns relevant to divertor loads, transport of impurities, plasma detachment, X-point radiation should be accurately determined to improve both operation and scientific exploitation of the experiments. Crucial information, related to instabilities potentially triggering disruptions, can also be derived from radiation anomalies.

As the radiation profile is, in general, highly non-uniform, tomography reconstruction of bolometry represents a solution for deriving its spatial 2D distribution. Bolometry measurements are provided by pinhole cameras, which are located roughly in a 2D poloidal cross section. The pinholes determine a set of line-of-sights (LOS), which define the geometry of the tomography problem. Figure 1 shows the ASDEX Upgrade (AUG) LOSs geometry. A detailed description of the AUG bolometry system is provided in [2, 3].

Given the access restrictions and the fact that bolometry must coexist with other diagnostics installed around the tokamak main chamber, in general a limited number of measurements are available. Therefore, due to the limited data availability, the tomography problem is mathematically ill-posed. In order to compensate for the lack of information, the reconstruction methods incorporate a regularizing procedure that assumes smoothness

Figure 1. Schematic view of AUG bolometric diagnostic layout.
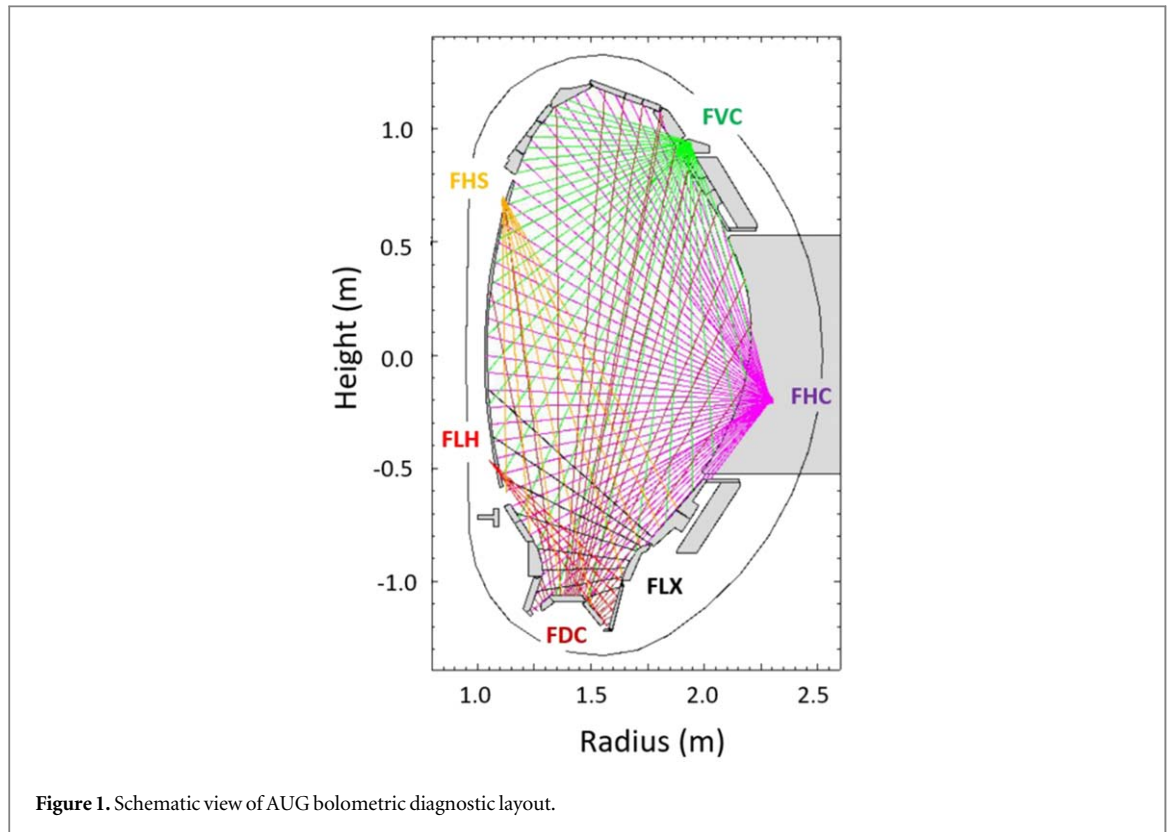
along the magnetic surfaces, given by the plasma equilibrium. The incorporation of the prior information, related to the magnetic configuration, plays an essential role in ensuring accurate reconstructions.

The reconstruction method used for routine bolometry analysis in AUG has been initially proposed in [4]. It is based on the minimisation of the chi-squared error between measured and back-calculated tomographic projections, with a regularization integral that describes the curvature of the 2D profile. The method implements also a regularisation procedure based on anisotropic smoothing, taking into account the asymmetric gradients of the radiation parallel and radial to the magnetic flux surfaces. Subsequent improvements have been proposed in [2]. The specific definition of the algorithm parameters for different regions (confined plasma, SOL inner and outer divertor, X-point) allow the minimisation of various artefacts and ensure increased robustness against experimental noise and dead channels. Recently, ray-tracing techniques have been applied to take into account the effect of the finite collection volume of the detector's apertures [5]. To optimise the computation of both total and local radiated power, a method based on tomography using a reduced reconstruction grid and the use of integrated values of radiation over large enough regions, averaging potential numeric artefacts, has been proposed in [6]. Very recently the application of Gaussian process tomography [7] to the bolometer diagnostic at ASDEX Upgrade has been reported [8]. This approach uses nonstationary Cartesian kernels and kernels that incorporate magnetic equilibrium information. The kernel hyperparameters are derived by a training process which is based on a subset of pre-existent AUG reconstructions, obtained with the method described in [2–4]. When using the nonstationary Cartesian kernel, which does not take into account the magnetic information, the computational speed is compatible with real-time application. The calculation of the reconstruction uncertainties is possible by using a certain error model for the measurements error. This model assumes that the detectors values are given by a constant background noise and a signal dependent noise. The parameters of these two additive components are derived by analysing a large collection of signals.

In the present paper, we propose to apply to AUG bolometry a reconstruction method based on the statistical Maximum Likelihood (ML). ML tomography has been already applied in JET for gamma, neutron, HXR tomography [9–11] and also for bolometry [12]. The advantage of the ML method is the capability of evaluating the reconstruction uncertainties when calculating the total radiated power or power profiles. The proper assessment of the uncertainties is, for example, an important aspect for investigating high radiative discharges [13]. Comprehensive studies regarding the uncertainties in bolometric tomography on JET have been reported [14, 15].

Sections 2–4 of the paper present a review of the ML tomographic method, from the point of view of its implementation on AUG. Details about the new smoothing procedure, used for regularising the ill-posed tomography problem, are also provided. The overall quality of the method has been assessed by numerical

simulations with phantoms and compared with the AUG standard method [2–4] as described in section 5. Representative results, obtained during AUG experiments, are also reported. Conclusions and the potential additional applications of the methodology are discussed in the last section of the paper.

2. Maximum likelihood reconstruction method

The expectation–maximization (EM) algorithm was proposed by Dempster *et al* [16] for problems, in which latent variables (not directly observed) have to be predicted, based on a set of observed data, assuming that the probability distribution associated with the latent variables is known.

Let be G the random vector containing the data measured in the experiment and $D^G(G, \theta)$ its density function, where θ are parameters to be estimated. Also let be F the vector in a larger space, embedding the sample space G. Therefore, a many-to-one mapping $G = h(F)$ exists. It is assumed also that F has the density function $D^F(F, \theta)$ with respect to a measure $\mu(F)$. $D^G(G, \theta)$ can be retrieved by integrating:

$$D^G(G, \theta) = \int D^F(F, \theta) d\mu(F) \tag{1}$$

or, in discrete form:

$$D^G(G, \theta) = \sum D^F(F, \theta) \tag{2}$$

At each iteration the EM algorithm, perform two successive steps. The first is the E-step when the conditional expectation:

$$E(\ln D^F(F, \theta) | G, \theta^{(k)}) \tag{3}$$

is created using the current estimation $\theta^{(k)}$ of the parameters. In the following M-step, the conditional expectation E is maximized with respect to θ in order to obtain the new estimates.

For emission tomography, the experimental measurements g are integrals over the emissivity distribution f taken along a set of lines of sight. The probability of detecting emission in detector m from pixel n is given by so called projection matrix $H = \{H_{mn}\}_{m=1,\ldots,M;n=1,\ldots,N}$, where M is the total number of detectors and N is the total number of pixels in the image representing the emissivity distribution. The projection matrix incorporates the detection geometry and other characteristics of the system. The tomography reconstruction problem can be formulated as follows:

$$g_m = \sum_{n=1}^{N} H_{mn} f_n \tag{4}$$

Let X_{nm} be the random number of photons that are emitted from pixel n and contribute to the measurement at detector m. The mean of X_{nm} is $H_{mn} f_n$. Also let Y_m be the total number recorded at detector m. Obviously $Y_m = \sum_n X_{nm}$.

It is assumed that the emissivity is governed by a spatial Poisson process. As measurements are linear combination of emissivities, they are also Poisson distributed. The log-likelihood function is given by the following equation (the reader is referred to [17, 18] for complete details about deriving this equation):

$$\ln D^F(Y, f) = \sum_m \{-\sum_n H_{mn} f_n + Y_m \ln(H_{mn} f_n) - \ln Y_m\} \tag{5}$$

Considering the conditional expectation of X_{mn} with respect to Y_m and the current vector of parameter estimates $f^{(k)}$, we have:

$$E(\ln D^F(X, f) | Y, f^{(k)}) = \sum_m \sum_n \{-H_{mn} f_n + Q_{mn} \ln(H_{mn} f_n) + R\} \tag{6}$$

where:

$$Q_{mn} = E\left(X_{mn} | Y_m, f^{(k)} = \frac{H_{mn} f_n^{(k)} Y_m}{\sum_l H_{ml} f_l^{(k)}}\right) \tag{7}$$

and R is a term which groups all the terms not depend on the new f values.

The M-step consists of equating to zero the partial derivatives of (7):

$$\frac{\partial}{\partial f_n} E(\ln D^F(X, f) | Y, f^{(k)}) = -\sum_m H_{mn} + \sum_m Q_{nm} f_n^{-1} = 0 \tag{8}$$

Which leads to the following equation for retrieving updated estimation:

$$f_n^{(k+1)} = \frac{\sum_m Qij}{\sum_m H_{mn}} = \frac{f_n^{(k)}}{\sum_m H_{mn}} \sum_m \frac{H_{mn} g_m}{\sum_j H_{mj} f_j^{(k)}} \tag{9}$$

It has to be noted that the non-negativity constraint $f_n^{(k)} \geqslant 0$ is ensured automatically.

3. Smoothing for reconstruction regularization

Due to the topology of the emission and the limited number of views, the bolometry problem is a highly underdetermined inversion. To compensate for the lack of experimental data, additional prior information must be used. A usual approach for regularizing the ill-posed problem is to assume smoothness along the magnetic surfaces, given by plasma equilibrium.

In the present approach, the smoothing operator is implemented based on the anisotropic smoothing techniques. For a systematic description of the theoretical foundations and of numerical aspects of this class of image smoothing methods, the reader is referred to [19]. Anisotropic smoothing has been first proposed by Perona-Malik [20] as a way to smooth images in a non-linear way with the aim of preserving image discontinuities which are blurred by various factors (noise, scratches, compression artefacts, etc). In general, the image is smoothed locally in several directions while the directions may vary from point to point. The directions are chosen to be parallel to the image contours in order to preserve the image edges.

In a first step the geometrical structure of the edges have to be determined. The geometry of the image F can be described by:

- two unit vectors: $\phi_{(X)}^+$ and $\phi_{(X)}^-$ directed along the local maximum and minimum variations of image intensities at location X; $\phi^- = \nabla f_\sigma^\perp / \|\nabla f_\sigma\|$ gives the contour direction and $\phi^+ = \nabla f_\sigma^\| / \|\nabla f_\sigma\|$ is related to the variation in the direction perpendicular on the contour.

- two corresponding positive values $\lambda_{(X)}^+$ and $\lambda_{(X)}^-$, measuring the effective variations of the image intensities along $\phi_{(X)}^+$ and $\phi_{(X)}^-$ respectively. $\lambda_{(X)}^+$ and $\lambda_{(X)}^-$ describe the local strength of the edge; the usual representation of these effects uses an ellipse with axis lengths corresponding to $\phi_{(X)}^+$ and $\phi_{(X)}^-$, and axis magnitudes given by λ^+ and λ^-. When $\lambda^+ \cong \lambda^-$, the neighbourhood is isotropic, while when $\lambda^+ \gg \lambda^-$, then the gradients in the local image region have the same orientation.

The image geometry $\{ \boldsymbol{\lambda}^{+/-}, \boldsymbol{\phi}^{+/-} \mid \boldsymbol{X} \}$ can be retrieved by computing the gradient field $\boldsymbol{\nabla f}$. A common approach is to use a smoothed gradient field $\boldsymbol{\nabla f_\sigma} = \boldsymbol{\nabla} \ f \times \boldsymbol{Gauss_\sigma}$, where $\boldsymbol{Gauss_\sigma}$ is a 2D Gaussian kernel with a variance $\boldsymbol{\sigma}$, in order to remove the noise effects.

A convenient way to work with the image geometry is to use the tensor $T(x) = \lambda^- \phi^- \phi^{-T} + \lambda^+ \phi^+ \phi^{+T}$; λ^- and λ^+ are the eigenvalues of T, while ϕ^- and ϕ^+ are the corresponding eigenvectors. Therefore, the local geometry of the image F is described by the tensor $T(x) = \nabla \ I_{(X)} \nabla \ F_{(X)}^T$.

A more flexible particular form of the field of diffusion tensors has been proposed in [18]:

$$T(x) = h_{(\lambda^+, \lambda^-)}^- \phi^- (\phi^-)^T \lambda^- + h_{(\lambda^+, \lambda^-)}^+ \phi^+ (\phi^+)^T \tag{10}$$

where the functions $h^{+/-}$ determines the strength of the smoothing along the directions ϕ^-, ϕ^+. Several choices of these functions are possible depending on the specific application. A possible choice is:

$$h_{(\lambda^+, \lambda^-)}^- = \frac{1}{(1 + \lambda^+ + \lambda^-)^{p_1}}, \quad h_{(\lambda^+, \lambda^-)}^+ = \frac{1}{(1 + \lambda^+ + \lambda^-)^{p_2}}, \, p_1 < p_2 \tag{11}$$

where p_1, p_2 are two adjustable parameters.

For a pixel located on the image contour, λ^+ has a high value and therefore $h^- \ll h^+$. Consequently, the smoothing along ϕ^-, it means along the contour, will prevail. For pixels located in a homogenous region, the smoothing will be performed isotopically as λ^+ has a small value and consequently $h^+ \simeq h^-$.
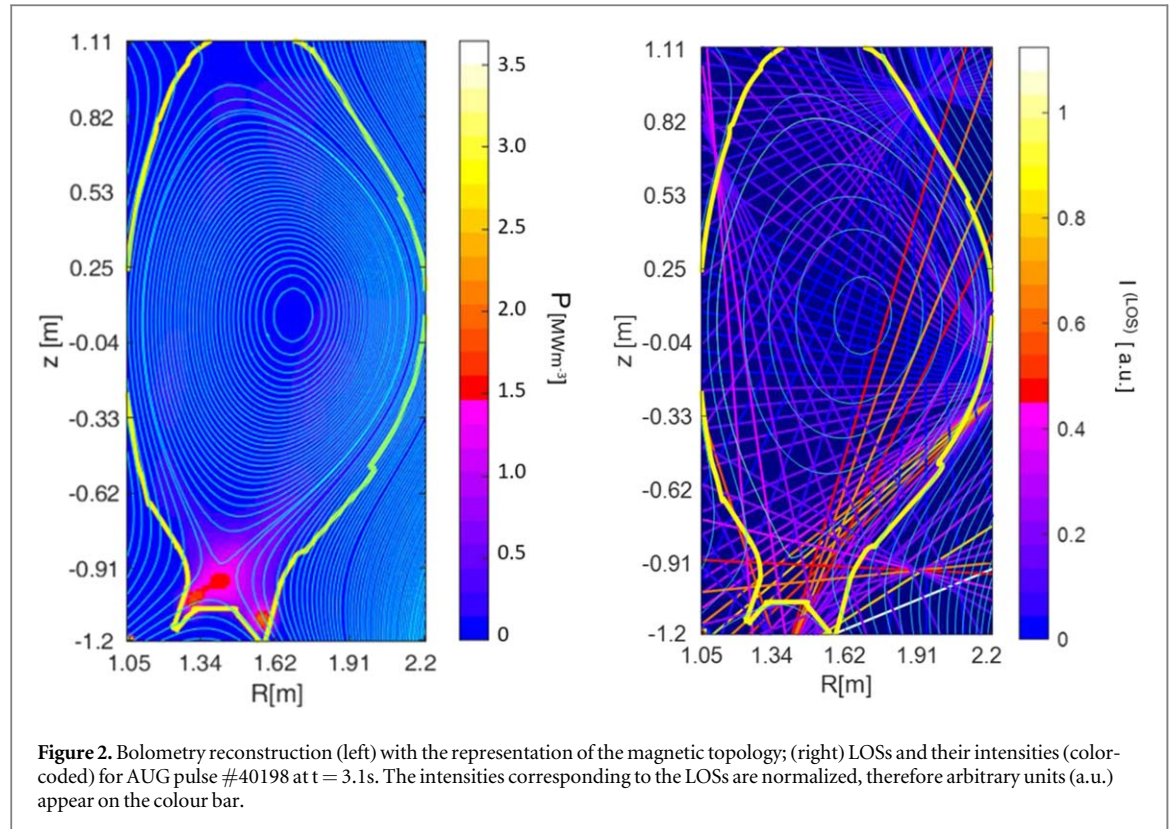
The anisotropic smoothing of the image F for the local geometry described by T can be formulated as a divergence PDE (Partial Differential Equations) problem [19]:

$$\frac{\partial F_i}{\partial t} = div(T \nabla \ F_i) \tag{12}$$

An alternative to the divergence equation (12) is a formulation based on a trace operator [21]:

$$\frac{\partial F_i}{\partial t} = trace(TH_i) \tag{13}$$

where $H_i = \begin{pmatrix} \frac{\partial^2 I_i}{\partial x^2} & \frac{\partial^2 I_i}{\partial x \partial y} \\ \frac{\partial^2 I_i}{\partial x \partial y} & \frac{\partial^2 I_i}{\partial y^2} \end{pmatrix}$ is the Hessian of F_i. As shown in [21], in this case, the smoothing is equivalent to the application of convolution around local values of X with a Gaussian mask $Gauss_t^T$, oriented by the tensor $T(x)$:

Figure 2. Bolometry reconstruction (left) with the representation of the magnetic topology; (right) LOSs and their intensities (color-coded) for AUG pulse #40198 at t = 3.1s. The intensities corresponding to the LOSs are normalized, therefore arbitrary units (a.u.) appear on the colour bar.

$$Gauss_t^T(x) = \frac{1}{4\pi t} \exp\left(-\frac{X^T T^{-1} X}{4t}\right) \tag{14}$$

For the bolometry images we followed the approach in [22] that considers an additional term in with respect to equation (13):

$$\frac{\partial F}{\partial t} = trace(ww^T H_i) + \nabla\, F_i^T J_w w \tag{15}$$

where w is the vector field used for smoothing: $\frac{w}{\|w\|}$ is the direction along which the smoothing is performed, while $\|w\|$ is the smoothing strength. Considering the two spatial components of w, $w_{(x)} = (u_{(x)}\ v_{(x)})^T$, then J_w stands for the Jacobian of w. This formulation takes into account the curvature of the smoothing directions. The image filtering is performed using curved Gaussian kernels, when necessary, for better preserving the image structure (the reader is referred to 20 for details).

In case of bolometry images, the image geometry and the diffusion tensors are not derived from the reconstructed image itself. As it is desired to favour smoothing along magnetic surfaces, the diffusion tensors are derived from the image representing the magnetic equilibrium (see figure 2). The anisotropic smoothing is applied during the reconstruction process (6) after each iteration.

4. Uncertainties estimation

Corrupting noise is always present in measured data and it may adversely affect the qualitative interpretation and quantitative analysis of the reconstructed images. Therefore, the accurate modelling of the projection noise propagation is an important issue. In general, the reconstruction methods applied for bolometry are based on highly non-linear algorithms, which make difficult the description of the image statistics. Also, multiple noise realizations are generally unavailable and therefore Monte Carlo approaches are not viable or at least very unreliable. On the contrary, the ML approach benefits from the significant effort that has been spent during time for developing methods for reconstruction uncertainty evaluation. Approximate formulas for the ensemble mean and covariance have been derived for the first time by Barret *et al* [23], various other developments being reported later [24–32].

The presence of noise in the data and in the reconstructed image is introduced by the relations:

$$g = \bar{g} + n_g \tag{16}$$

$$\hat{f}^{(k)} = \overline{\overline{f}}^{(k)} + n_f^{(k)} \tag{17}$$

Where $\overline{g}$ and $\overline{\overline{f}}^{(k)}$ denotes the expectation of the data and image estimate, respectively, and n_g and n_f are zero mean noise vectors.

Following the above-mentioned approaches, the ML tomography problem can be formulated as a maximization problem:

$$\hat{f} = argmax_f \ L(g|f) \tag{18}$$

A preconditioned gradient ascent algorithm solver can be written as:

$$\hat{f}^{(k+1)} = \hat{f}^{(k)} + \alpha C^{(k)}(\hat{f}^{(k)}) \nabla_x \ L(g|f) \tag{19}$$

where $\alpha > 0$ is a fixed step size, $C^{(k)}(\hat{f}^{(k)})$ is a positive definite matrix (pre-conditioner), normally a function of the current image estimate. The typical pre-conditioner used for ML tomography is: $\alpha C^{(k)}(\hat{f}^{(k)}) = diag[\hat{f}^{(k)}] diag[s^{-1}]$, where s is a vector with all elements equal to 1 [27].

The first main assumption in deriving a formula for the reconstruction uncertainty, is the low magnitude of the noise level in the data, which allows a first-order Taylor expansion:

$$\nabla_x \ L(g| \ \hat{f}^{(k)}) \approx \nabla_x \ L(\overline{g}| \ \overline{\overline{f}}^{(k)}) + \nabla_{xy} \ L(\overline{g}| \overline{\overline{f}}^{(k)})n_g + \nabla_{xx} \ L(\overline{g}| \ \overline{\overline{f}}^{(k)})n_f \tag{20}$$

$$C^{(k)}(\hat{f}^{(k)}) \approx C^{(k)}(\hat{f}^{(k)}) + C_x^{(k)}(n_f^{(k)}, \hat{f}^{(k)}) \tag{21}$$

Substituting (20) and (21) into (19) and separating the signal from noise, the following equations can be obtained:

$$\hat{f}^{(k+1)} \approx \hat{f}^{(k)} + \alpha C^{(k)}(\hat{f}^{(k)}) \cdot \nabla_x \ L(\bar{g}|\overline{\overline{f}}^{(k)}) \tag{22}$$

$$n_f^{(k+1)} \approx [I - A^{(k)}]n_f^{(k)} + B^{(k)}n_g = V^{(k+1)}n_g \tag{23}$$

where:

$$A^{(k)} = -\alpha C^{(k)}(\hat{f}^{(k)}) \cdot \nabla_{xx} \ L(\overline{g}|\overline{\overline{f}}^{(k)}) - \alpha M \nabla_x \ L(\overline{g}|\overline{\overline{f}}^{(k)}), \tag{24}$$

$$B^{(k)} = \alpha C^{(k)}(\hat{f}^{(k)}) \cdot \nabla_{xy} \ L(\overline{g}|\overline{\overline{f}}^{(k)}) \tag{25}$$

and where the (j, l) element of $M[g; f]$ is $\sum_m g_m \partial C_{jm}^k(f)/\partial f_l$.

Equation (22) shows that the image reconstruction expectation can be obtained using the measured data expectation while equation (23) represents a linear update formula for the reconstruction uncertainty. It has to be emphasised again that both equations hold if the magnitude of the noise accompanying the measured data is low.

Equation (23) can be re-written in the form:
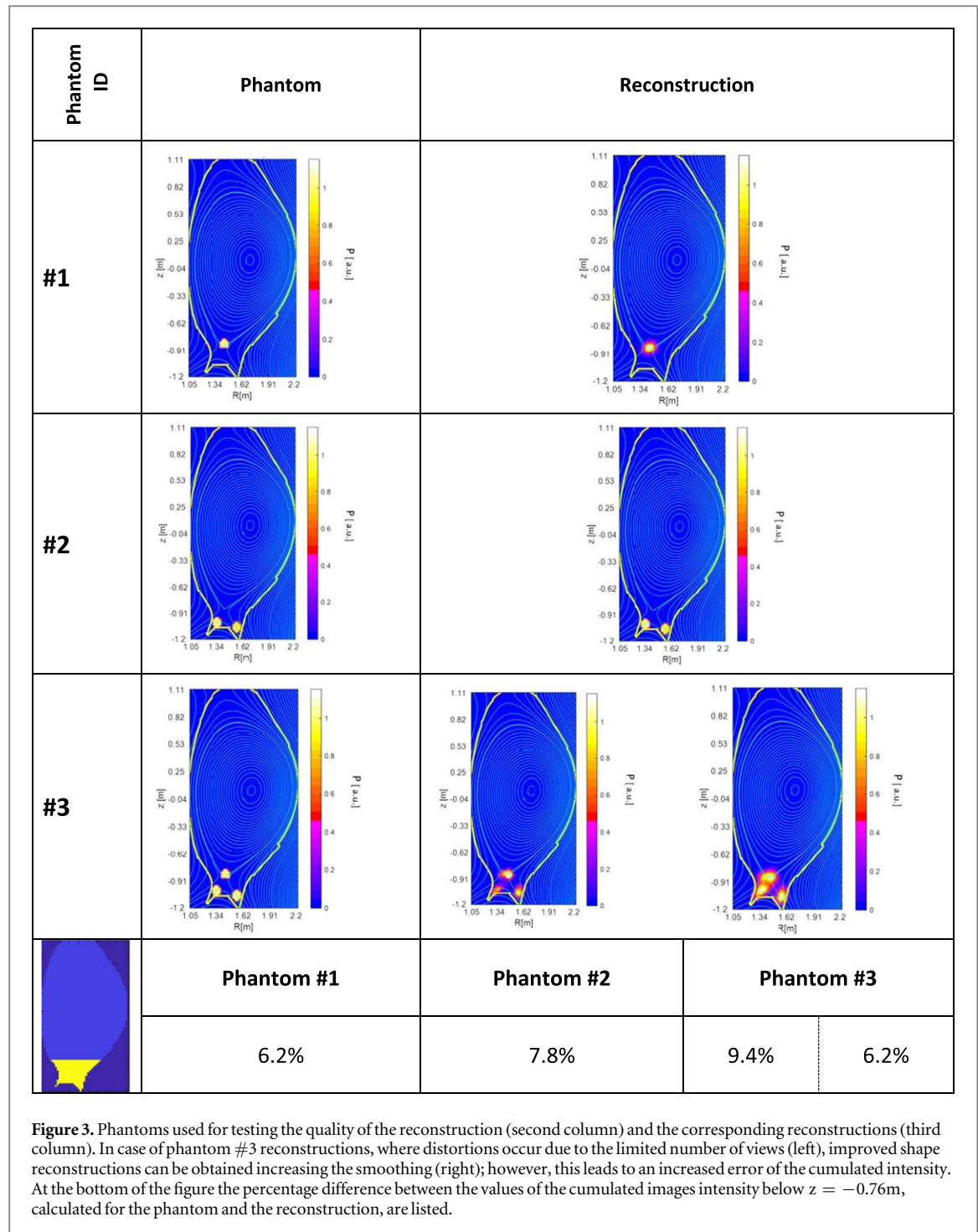
$$V^{(k+1)} = [I - A^{(k)}]V^{(k)} + B^{(k)} \tag{26}$$

which allows the derivation of the reconstruction covariance:

$$COV(\hat{f}^{(k)}) = V^{(k)}COV(g)[V^{(k)}]' \tag{27}$$

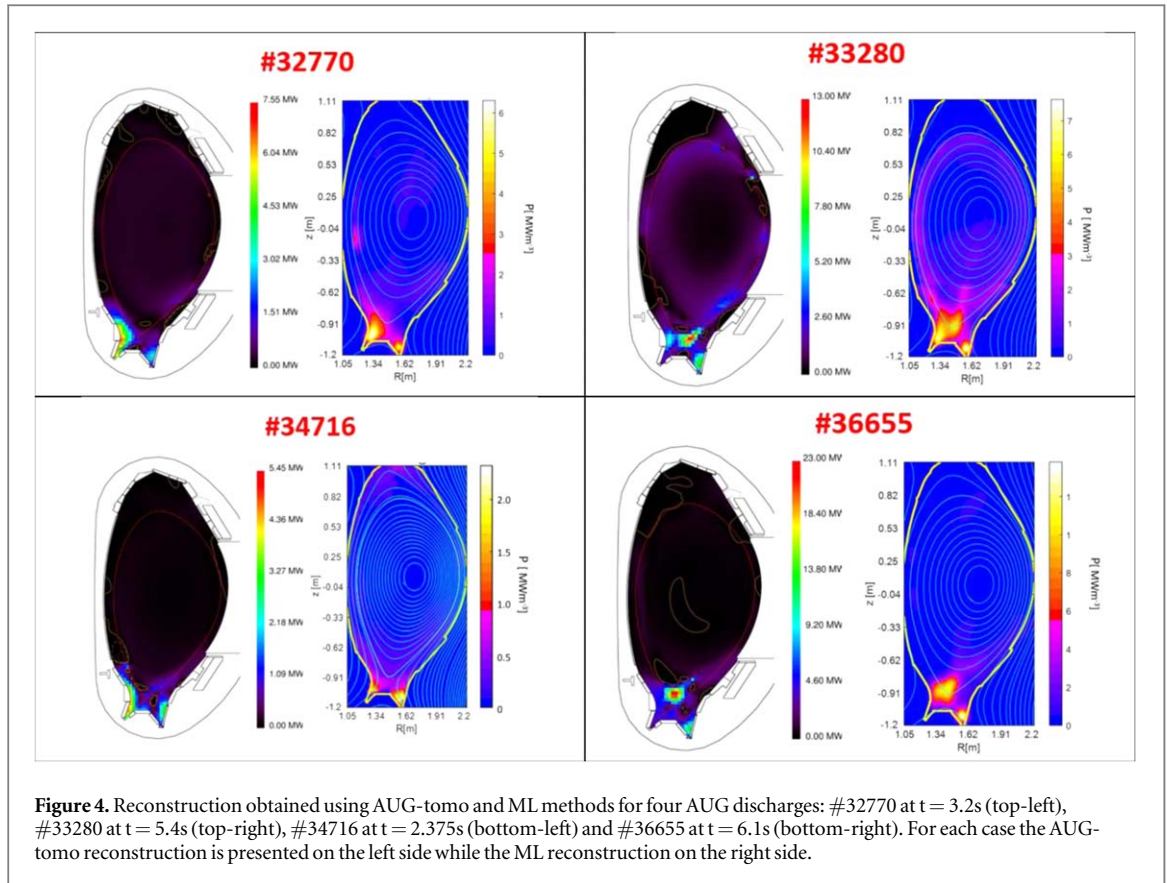where $COV(g)$ is the covariance of the measured data.

5. Results

The performances of the ML bolometry reconstruction method for AUG have been assessed with a set of phantoms. The phantoms are created as combinations of discs of diameter equal to 0.1 m, lying on a 5% background. These combinations are mimicking experimental cases (see below in this paper). For each phantom, the corresponding tomographic projections are calculated using equation (4), simulating the measurement process. Then, the phantom projections are used by the ML code to obtain tomography reconstructions which are compared with the phantoms in order to assess the performances of the method. The phantoms, together with their reconstructions, are presented in figure 3. Beside the qualitative comparison, a quantitative evaluation has been performed by calculating the cumulated image intensities in the region where the image features are located. This region is defined as the set of pixels located below Z = −0.76 m. This limit defines the radiative region located below the X-point. The limit, used throughout the paper, is located slightly above the X point height, in order to allow the inclusion of possible radiation spots located at the X-point. The percentage differences are presented also in figure 1. From the tomographic point of view, the phantom #3 represents the most difficult case. Each disc of the phantom is in the shadow of the others with respect to

Phantom ID	Phantom	Reconstruction
#1		
#2		
#3		

	Phantom #1	Phantom #2	Phantom #3	
	6.2%	7.8%	9.4%	6.2%

Figure 3. Phantoms used for testing the quality of the reconstruction (second column) and the corresponding reconstructions (third column). In case of phantom #3 reconstructions, where distortions occur due to the limited number of views (left), improved shape reconstructions can be obtained increasing the smoothing (right); however, this leads to an increased error of the cumulated intensity. At the bottom of the figure the percentage difference between the values of the cumulated images intensity below $z = -0.76$m, calculated for the phantom and the reconstruction, are listed.

different LOSs. Due to the limited number of asymmetric views, certain distortions in the reconstruction of disks shape occur. The shape reconstruction can be improved by an increased smoothing but the price paid is the increased error in the value of the cumulated intensity (equivalent to radiated power for real experiments). In practice the real shape of the radiation distribution is, of course, unknown. Therefore, the smoothing parameters should be slightly varied and then the final reconstruction could be chosen by correlating its shape with independent physical aspects, when possible. As the isotropically smoothing does not make sense for the particular structure of the phantoms in figure 3, we used a Gaussian smoothing filter of size 5×5. Further numerical tests will be performed, using phantoms with shapes mimicking the distribution encountered in experiments.

The performances of the method have been evaluated also by means of a comparison with the results provided by the reconstruction method used routinely for bolometry analysis on this device (noted for the rest of the paper as AUG-tomo [4]). The comparison has been performed for a set of four cases, selected for being exemplary for different radiation patterns, from the tomographic point of view. The experimental data has been

Figure 4. Reconstruction obtained using AUG-tomo and ML methods for four AUG discharges: #32770 at t = 3.2s (top-left), #33280 at t = 5.4s (top-right), #34716 at t = 2.375s (bottom-left) and #36655 at t = 6.1s (bottom-right). For each case the AUG-tomo reconstruction is presented on the left side while the ML reconstruction on the right side.

measured in the following experiments: discharge #32770 at t = 3.2 s (experiment with He as main species), discharge #33280 at t = 5.4 s (high radiation scenarios experiment with Ar seeding), discharge #34716 at t = 2.375 s (low density, no seeding, reference scenario) and #36655 at 6.1 s (X-point control and detachment characterization experiment with N seeding). The bolometry reconstructions obtained using AUG-tomo and ML methods are presented in figure 4. The reconstructions display radiative spots developing at the X-point or on the divertor tiles. The most complicated case is for the discharge #33280 where a radiating zone develops inside the separatrix, slightly above the X-point, after divertor detachment. Figure 4 shows that the ML method is able to correctly identify the radiative patterns, in terms of shapes and resolution, in all cases.

Beside the qualitative comparison between the AUG-tomo and ML methods, a quantitative evaluation of the radiation emitted in different regions has been performed. Four regions have been defined for this quantitative comparison, as illustrated in figure 5. The values of the radiated powers, calculated using the AUG-tomo and ML methods are presented in table 1. The values show a good agreement between the two methods.

As already mentioned, the specific advantage of the ML method is related to the calculation of the reconstruction uncertainties, based on the statistical uncertainties of the measured data. For each time instance t the measured data is read in an interval $[t - 5ms, t + 5ms]$ and the mean and standard deviation are calculated. Outliers are identified based on the scaled median absolute deviation and excluded [14]. The image variances, corresponding to each reconstruction, are presented in figure 6 for the four analysed cases. The shape of the image variance is, in general, similar to the shape of the reconstruction. As remarked for the first time by Llacer *et al* [31], ML-EM algorithms are characterised by a monotonically increasing dependence of the noise variance on the mean (or noise-free) image pixel values. This is an advantageous characteristic of the ML method. In case of linear methods, for example, the noise in the high-intensity regions tend to contribute to relatively distant low-intensity regions [32]. However, this similarity is perturbed when part of the input measured values have a significantly increased statistical uncertainty, as, for example, in the case of #32770 discharge (figure 6 first line and figure 7).

The image variance allows the calculation of the uncertainties related to each derived quantity depending on the emission distribution. Quantifying the uncertainties in the reconstructions on a routine basis would be beneficial for various studies. For example, an accurate estimate of the uncertainties is essential when approaching high radiation fraction from the point of view of both the plasma control and the interpretation of the physics. An accurate evaluation of the radiated powers in different locations of the main chamber, together with the associated uncertainties, proved to be a useful tool in analysing the dynamics of the radiation leading to
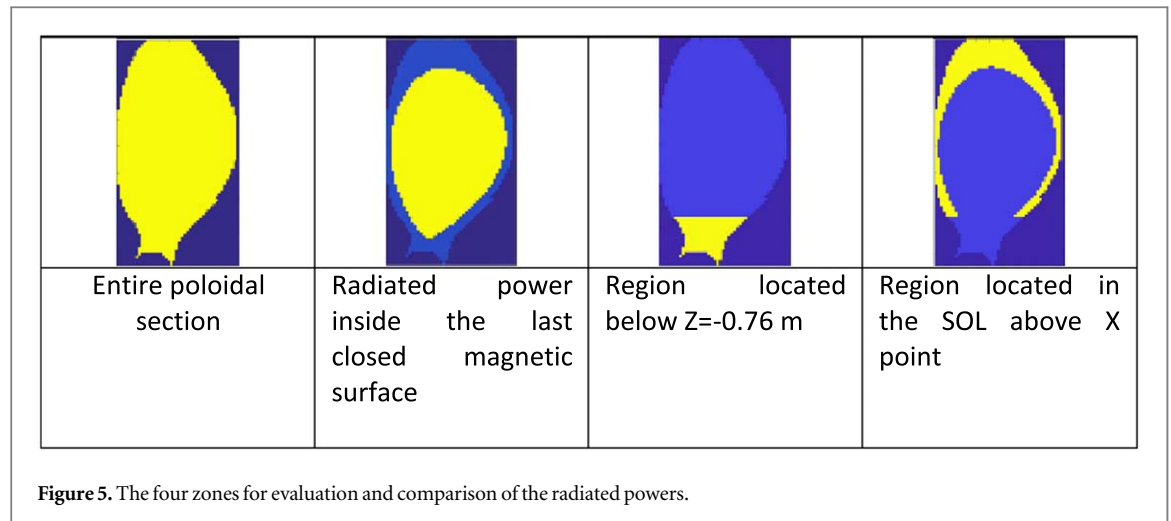
Figure 5. The four zones for evaluation and comparison of the radiated powers.
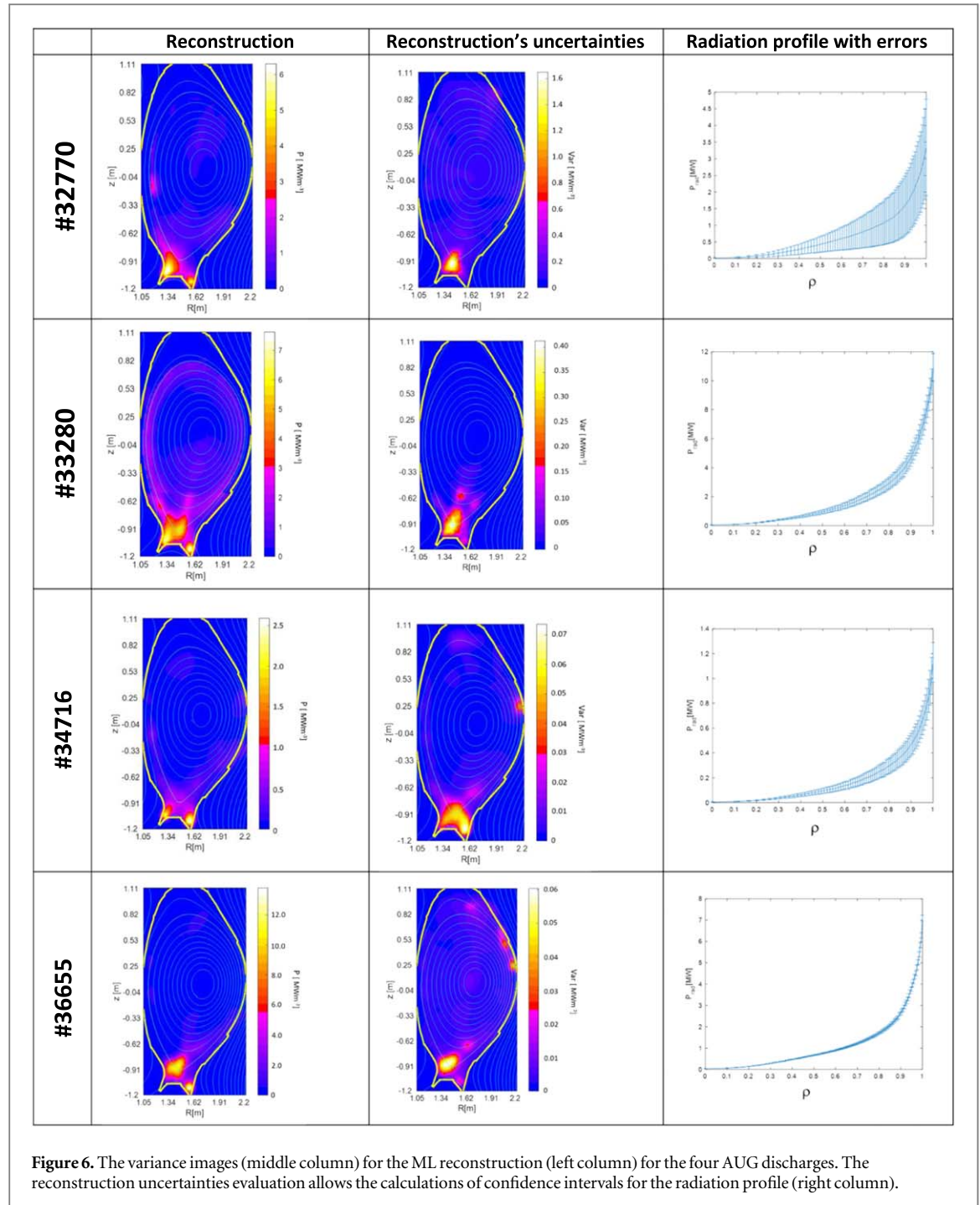
Table 1. Comparison between the values of the radiated powers, in different poloidal regions, calculated with the AUG-tomo and ML methods.

	Radiated power from the entire poloidal section	Radiated power inside the last closed magnetic surface	Radiated power below $Z = -0.76$ m	Radiated power in the SOL above Xp
		#32770		
P (MW) AUG-tomo	6.13	3.14	2.78	0.47
P (MW) ML	6.11	2.82	2.49	0.54
Difference	−0.4%	−11.4%	−11.5%	12.2%
		#33280		
P (MW) AUG-tomo	14.53	10.36	4.26	1.45
P (MW) ML	15.98	10.39	4.33	1.63
Difference	9.05%	−11.38%	1.63%	10.93%
		#34716		
P (MW) AUG-tomo	3.38	0.99	2.17	0.39
P (MW) ML	3.02	1.14	1.90	0.44
Difference	−11.98%	12.59%	−13.93%	10.60%
		#36655		
P (MW) AUG-tomo	12.58	7.47	7.51	1.20
P (MW) ML	13.61	7.05	6.69	1.30
Difference	7.53%	−5.98%	−12.29%	7.83%

disruptions in a series of discharges with impurity seeding, devoted to the investigation of high radiated fraction regimes [13]. For routine analysis, the availability of the reconstruction statistical uncertainty permits the calculation of error bars for the power profiles, as illustrated in figure 6 (last column). The power profiles are evaluated using the reconstruction image. Each value of the radiation profile represents the total radiation calculated inside the corresponding magnetic surface ρ; $\rho = 0$ at the centre of the plasma while $\rho = 1$ at the last closed magnetic surface. The error bars are evaluated accordingly, using the reconstruction variance.

A significantly increased value of the error bars is obtained in case of the #32770 discharge, due to the relatively large number of experimental data points with high statistical uncertainty value (figure 7). The evaluation of the uncertainties corresponding to the radiated power calculated for the four zones defined in figure 5 is given in table 2. The uncertainty values account only for the statistical uncertainties, the systematic errors have not been considered.

Figure 6. The variance images (middle column) for the ML reconstruction (left column) for the four AUG discharges. The reconstruction uncertainties evaluation allows the calculations of confidence intervals for the radiation profile (right column).

As already stated, for the reconstruction in figure 6, the measured data is read in an interval of 10 ms. The use of such a low value is advantageous when the radiation distribution changes fast. On the other hand, it implies high statistical uncertainties. When the radiation distribution is stable, it is, of course, better to use higher temporal intervals for collecting data, in order to ensure lower variances. An example is presented in figure 8 for the pulse #34716. The temporal interval has been set at 150ms. It can be observed that the image variance becomes more similar with the reconstruction image. Also, the error bars for the radiation profiles diminishes. Therefore, the evaluation of the reconstruction statistical uncertainties could be a helpful instrument for making a good compromise between the level of the error bars and the tomography time resolution. In certain cases, the choice of a large temporal window, ensuring low variances, in not possible due to the fast variation of the radiation distribution. An example is presented in figure 9.

The projection data collected when using a window of 10 ms and of 150 ms, respectively, is very different, leading to different shapes of the reconstruction. For the window of 150 ms, the associated variance (not shown in figure 9) incorporates a component due to inherent statistical variations but also a component determined by the variation of the radiation distribution. As the use of a short time interval is necessary in this case, the
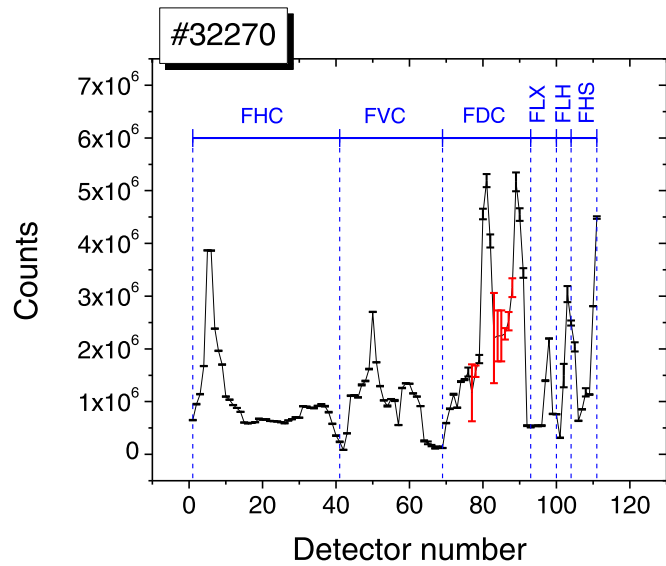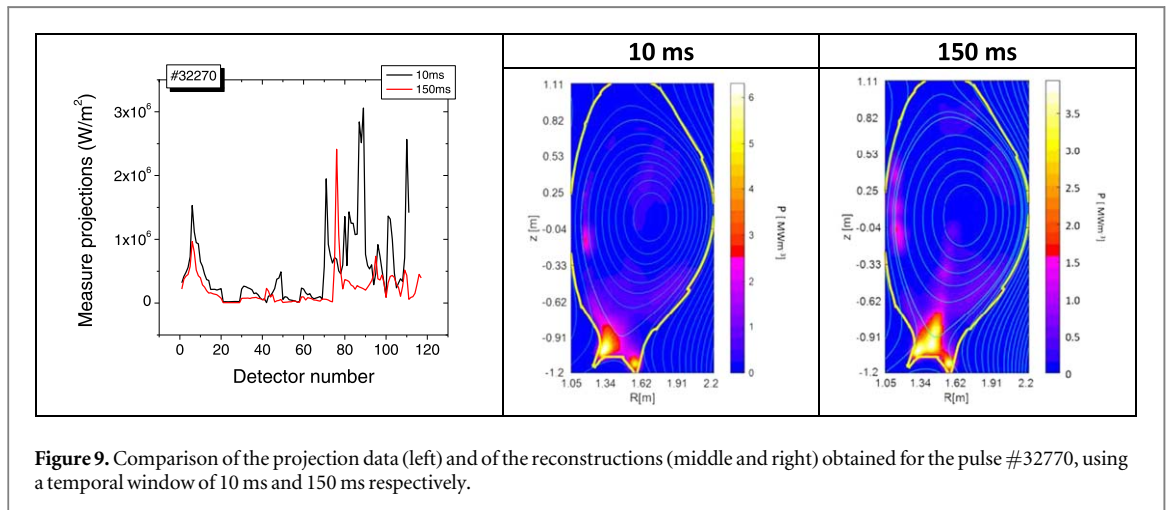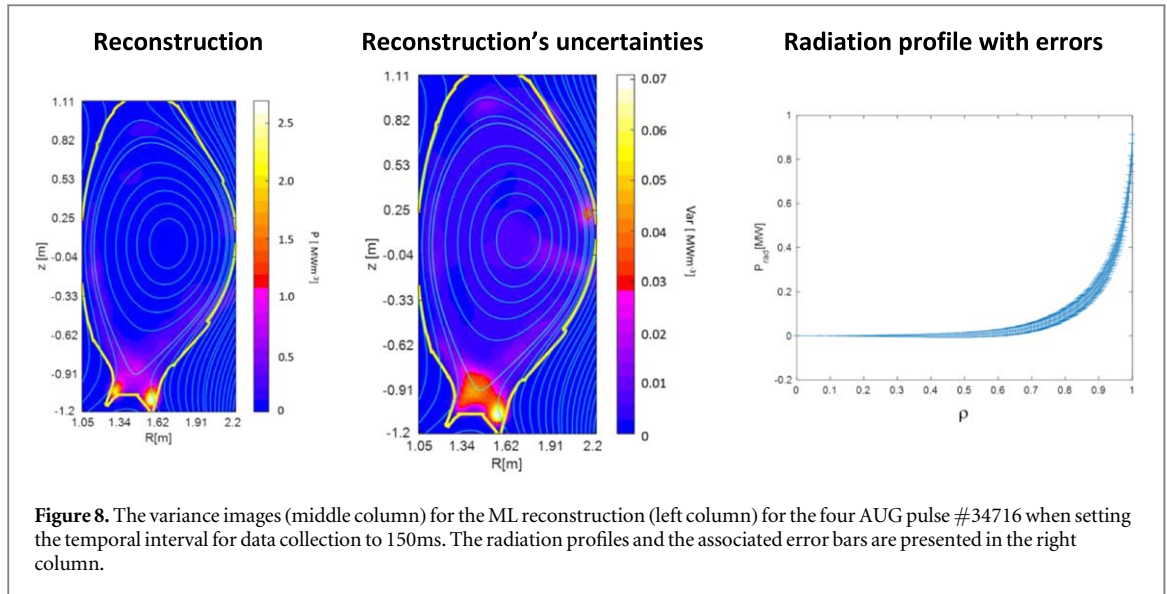
Figure 7. Measured data with statistical uncertainties for AUG discharge #32770. Data points with high uncertainty values are marked in red. The detectors belonging to different cameras are indicated in blue. The vertical dashed cyan bars mark the detectors involved in the creation of the spot highlighted in figure 10.

Table 2. ML power calculations and uncertainty evaluation in different poloidal regions.

	Radiated power from the entire poloidal section	Radiated power inside the last closed magnetic surface	Radiated power below Xp Z = −0.76	Radiated power in the SOL above Xp
		#32770		
ML power [MW]	6.11	2.82	2.49	0.54
Uncertainty	+/− 2.12	+/− 1.18	+/− 0.23	+/− 0.63
	34.7%	41.8%	20.0%	32.2%
		#33280		
ML power [MW]	15.98	10.39	4.33	1.63
Uncertainty	+/− 0.75	+/− 0.23	+/− 0.31	+/− 0.11
	4.7%	5.0%	7.2%	%
		#34716		
ML power [MW]	3.02	1.14	1.90	0.44
Uncertainty	+/− 0.32	+/− 0.16	+/− 0.04	+/− 0.10
	4.5%	4.4%	3.2%	4.9%
		#36655		
ML power [MW]	13.61	7.05	6.69	1.30
Uncertainty	+/− 0.21	+/− 0.13	+/− 0.01	+/− 0.05
	1.6%	1.9%	0.5%	1.9%

evaluation of statistical uncertainties of the reconstruction is important to judge the relevance of the features in the reconstruction.

Coming back to the comparison of the reconstruction provided by the ML and the AUG-tomo methods (table 1), it should be remarked that the differences between the radiated power values calculated for various regions of the main chamber do not exceed 16%. However, this value is higher than the reconstruction statistical uncertainties reported in figure 3. The explanation should focus on the limited data type tomography of bolometry. The high underdetermination is solved differently by the two methods. The additional differences, which cannot be accounted for by statistical uncertainties, give an idea about the limitations inherent in solving this tomography problem.

Figure 8. The variance images (middle column) for the ML reconstruction (left column) for the four AUG pulse #34716 when setting the temporal interval for data collection to 150ms. The radiation profiles and the associated error bars are presented in the right column.

Figure 9. Comparison of the projection data (left) and of the reconstructions (middle and right) obtained for the pulse #32770, using a temporal window of 10 ms and 150 ms respectively.

An example of a situation which is hard to be clarified due to the limited number of views is presented in figure 10, for the pulse #32770. The feature on the on the high-field-side midplane (encircled in figure 9) is outside the statistical error bars (see figure 6 first row). However, this image feature could be an artifact. The spot is in the shadow of the point located in the inner divertor region, being generated by the high values measured in the detectors corresponding to LOSs 88–89 in combination with the detector values corresponding to LOSs 55–56, which are a bit more elevated than the neighboring detectors. The LOSs contributing to the creatin of this spot are marked by cyan vertical bars in figure 7. As can be seen in figure 4, this situation is solved differently by the AUG-tomo and ML methods. Only an increased number of views, unfortunately unavailable, could clarify if this spot is an artifact or not.

The ML method has been used for the analysis of recent experiments. Two examples are presented in figures 11–12. The reconstruction in figure 11 shows the formation of a X-point radiator [33, 34] in case of the AUG discharge #40333. The reconstruction in figure 12 has been obtained during the discharge #40363, in an experiment dedicated to plasma detachment. The evolution in time of the bolometry reconstructions for these two cases is presented in the supplementary material in the form of videos. The videos have been obtained using a temporal resolution of 10 ms. The time interval investigated are: 1.0–8.0s for the discharge #40333 and 2.1–7.0s for the discharge #40363. Reconstruction time series may provide an overview of the pulse behaviour, mainly shortly after the experiment, followed later by detailed analysis of specific time instances, interesting for various physics phenomena.

The ML reconstruction method needs 10–15 iterations to converge. This takes a few tens of seconds on a usual computer in the MATLAB environment. As it has been recently shown, an accelerated version, implemented in C and using a compatible ITER fast controller platform with the Ubuntu 18.04 or the ITER
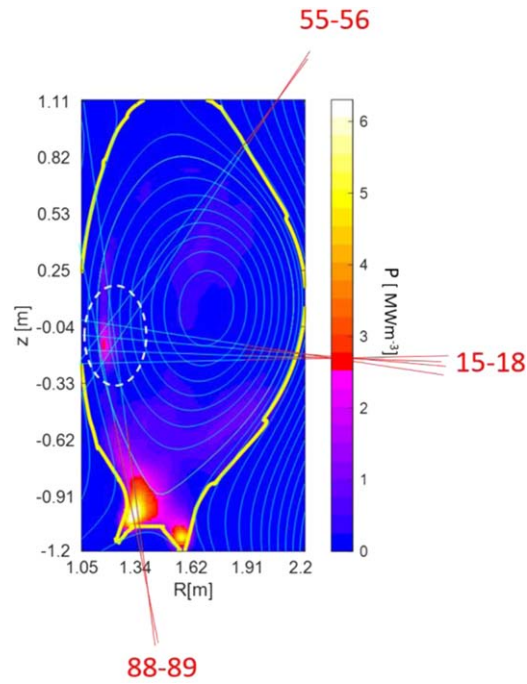
Figure 10. The LOSs (red-cyan lines) are responsible for the creation of a spot (white dashed encircled), which is difficult to be classified as a real feature or as an artefact. The detector measurements corresponding to these LOSs are marked by the dashed cyan vertical bars in figure 7.
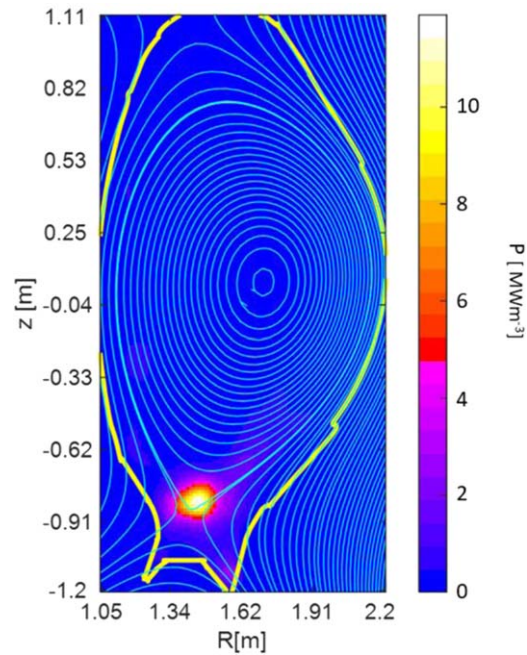

Figure 11. Reconstruction for the AUG discharge #40333 at t = 4.0 s. The reconstruction shows the formation of a X-point radiator.

Codac Core System distributions (6.1.2), achieves the final reconstruction in a few seconds [35]. Therefore, the method is compatible with inter-shot analysis.

The specific advantage of the ML reconstruction algorithm consists of the possibility to evaluate reconstruction statistical uncertainties. This evaluation is useful in various ways. First, the variance associated with different features in the image is a measure of the confidence regarding their real existence. However, reconstructions are affected not only by statistical uncertainties but also by artifacts generated by the limited data sets and by the reconstruction methods' imperfections. Therefore, the analysis of the reconstruction variance image is only a step in validating the reconstruction features. The level of the reconstruction uncertainties is
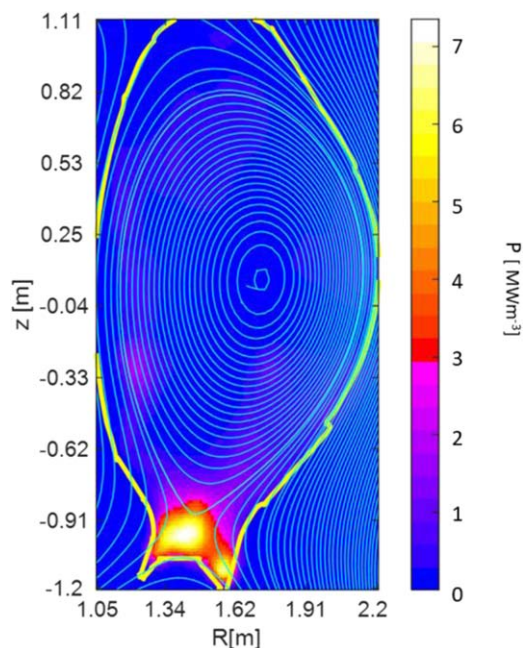
Figure 12. Reconstruction for the AUG discharge #40363 at t = 4.3 s, for a plasma detachment experiment.

directly correlated with the size of the window used for collecting data. Therefore, a good compromise between reasonable uncertainties and a good time resolution can be obtained based on this information. The dissimilarities between the shape of the reconstruction and of the image variance is an indicator that several detectors, viewing the regions with significant differences, are affected by increased statistical errors. The reconstruction variance image also allows the derivation of the confidence intervals for total radiated power, of for the power radiated in different regions of interest. Confidence intervals can be calculated for any other physical quantities derived from the radiation power distribution.

6. Conclusions

The tomographic inversion method based on the maximum likelihood has been applied to ASDEX Upgrade bolometry. The main advantage of the method is the ability to quantify the uncertainties of the tomographic reconstruction and of the derived quantities, such as the radiated powers in different locations of the main chamber and radiation profile, given the actual instrumental errors of the diagnostic. A new anisotropic smoothing technique, acting along locally oriented kernels improves the quality of the tomograms.

The algorithm has been assessed by numerical tests with phantoms and tested with discharges related to different experiments, for which validated tomograms obtained with AUG standard tomographic code are available. The percentage difference does not exceed 16%. In some cases, this difference is higher than the statistical uncertainties associated to the ML tomograms. Apart from the noisy data, the final reconstructed image also depends on the constraints imposed by the diagnostic layout, which are solved in a different way by the two methods. The spread of the results provides information about the effects of the limited bolometric data sets.

Also, in terms of future developments, it is believed that, once finally adjusted, the ML tomographic technique could be a good complement to the traditional AUG algorithm. The competitive advantage of providing confidence intervals in the reconstructions on a routine basis, should help in many integral parts of AUG programme, from detachment to the X-point radiator and the experiments with impurity seeding. Given JET experience, an accurate determination of the radiation patterns could become also very useful to better understand and predict disruptions [13, 36].

Acknowledgments

Data availability statement

The data cannot be made publicly available upon publication because they are owned by a third party and the terms of use prevent public distribution. The data that support the findings of this study are available upon reasonable request from the authors.

ORCID iDs

Teddy Craciunescu ⬤ https://orcid.org/0000-0002-0012-4260
Emmanuele Peluso ⬤ https://orcid.org/0000-0002-6829-2180
Andrea Murari ⬤ https://orcid.org/0000-0002-3932-3865
Michela Gelfusa ⬤ https://orcid.org/0000-0001-5158-7292
Pierre David ⬤ https://orcid.org/0000-0003-4837-8507
Stuart Henderson ⬤ https://orcid.org/0000-0002-8886-1256
Olivier Fevrier ⬤ https://orcid.org/0000-0002-9290-7413

References

[1] Odstrcil M, Mlynar J, Odstrcil T, Alper B and Murari A 2012 Modern numerical methods for plasma tomography optimisation *Nucl. Instrum. Methods Res.* A **686** 156–61
[2] Bernert M 2013 Analysis of the H-mode density limit in the ASDEX Upgrade tokamak using bolometry, (https://core.ac.uk/download/pdf/210795049.pdf)
[3] Bernert M, Eich T, Burckhart A, Fuchs J C, Giannone L, Kallenbach A, McDermott R M and Sieglin B 2014 Application of AXUV diode detectors at ASDEX Upgrade *Rev. Sci. Instrum.* 53- **3** 104003
[4] Fuchs C, Mast K F, Herrmann A and Lackner K 1994 Two-dimensional reconstruction of the radiation power density in ASDEX upgrade *Europhysics Conf. Abstracts (Proc. of the 21th EPS Conf. on Controlled Fusion and Plasma Physics, Montpellier* 18B:1308–1311, 1994. e) (http://fusionwiki.ciemat.es/wiki/European_Physical_Society_Conference_on_Plasma_Physics)
[5] Carr M, Meakins A, Bernert M, David P, Giroud C, Harrison J, Henderson S, Lipschultz B and Reimold F 2018 Impact of ray-tracing techniques on bolometry inversions and total radiated power measurements at ASDEX Upgrade *Rev. Sci. Instrum.* **89** 083506
[6] David P, Bernert M, Pütterich T, Fuchs C, Glöggler S and Eich T 2021 Optimization of the computation of total and local radiated power at ASDEX Upgrade *Nucl. Fusion* **61** 066025
[7] Svensson J 2011 Non-parametric tomography using gaussian processes EFDA–JET–PR(11)24, European Fusion Development Agreement–JET, (https://scipub.euro-fusion.org/wp-content/uploads/eurofusion/EFDP11024.pdf)
[8] Moser K, Bock A, David P, Bernert M and Fischer R 2022 Gaussian process tomography at ASDEX upgrade with magnetic equilibrium information and nonstationary kernels *Fusion Sci. Technol.* **78** 607–16
[9] Craciunescu T, Bonheure G, Kiptily V, Murari A, Tiseanu I and Zoita V 2008 The maximum likelihood reconstruction method for JET neutron tomography *Nucl. Instrum. Methods Res.* A **595** 623–30
[10] Craciunescu T, Bonheure G, Kiptily V, Murari A, Tiseanu I and Zoita V 2009 A comparison of four reconstruction methods for JET neutron and gamma tomography *Nucl. Instrum. Methods Phys. Res.*A **605** 373–84
[11] Gelfusa M, Craciunescu T, Peluso E, Giacomelli L, Kiptily V, Reux C, Szepesi G and Murari A 2021 A maximum likelihood tomographic method applied to JET gamma ray emission during the current quench *Fusion Eng. Des.* **168** 112637
[12] Craciunescu T, Peluso E, Murari A and Gelfusa M 2018 Maximum likelihood bolometric tomography for the determination of the uncertainties in the radiation emission on JET TOKAMAK *Rev. Sci. Instrum.* **89** 053504
[13] Murari A, Peluso E, Craciunescu T, Lowry C, Aleiferis S, Carvalho P and Gelfusa M 2020 Investigating the thermal stability of highly radiative discharges on JET with a new tomographic method *Nucl. Fusion* 60- **4** 046030
[14] Peluso E, Craciunescu T, Murari A, Carvalho P and Gelfusa M 2019 A comprehensive study of the uncertainties in bolometric tomography on JET using the maximum likelihood method *Rev. Sci. Instrum.* 90-12 123502
[15] Peluso E, Gelfusa M, Craciunescu T, Martellucci L, Gaudio P, Carvalho P and Murari A 2022 Dealing with artefacts in JET iterative bolometric tomography using masks *Plasma Physics. Controlled. Fusion* **64** 045013
[16] Dempster A P, Laird N M and Rubin D B 1977 Maximum likelihood from incomplete data via the EM *algorithm, J. Roy. Stat. Soc., Ser.* B **39** 1–38
[17] Shepp L A and Vardi Y 1982 Maximum likelihood reconstruction in positron emission tomography *IEEE Trans. Med. Imag.* **1** 113–22
[18] Lange K and Carson R 1984 EM reconstruction algorithms for emission and transmission tomography *J. Comp. Ass. Tomogr.* **8** 302–16
[19] Weickert J 1998 *Anisotropic Diffusion in Image Processing* (Stuttgart: Teubner Verlag)
[20] Perona P and Malik J 1990 Scale-space and edge detection using anisotropic diffusion *IEEE Trans. Pattern Anal. Mach. Intell.* **12** 629–39
[21] Tschumperlé D and Deriche R 2005 Vector-valued image regularization with PDE's: a common framework for different applications *IEEE Trans. Pattern Anal. Mach. Intell.* **27** 506–17
[22] Tschumperlé D 2006 Fast Anisotropic smoothing of multi-valued images using curvature-preserving PDE's *Int. J. Comput Vis.* **68** 65–82
[23] Barrett H H, Wilson D W and Tsui B M W 1994 Noise properties of the EM algorithm. I *Theory, Phys. Med. Biol.* **39** 833–46

[24] Fessler A and Rogers W L 1996 Spatial resolution properties of penalized likelihood image reconstruction: space invariant tomographs *IEEE Trans. Image Process.* **5** 1346–58

[25] Wang W and Gindi G 1997 Noise analysis of MAP-EM algorithms for emission tomography *Phys. Med. Biol.* **42** 2215–32

[26] Soares E J, Byrne C L and Glick S J 2000 Noise characterization of blockiterative reconstruction algorithms. I. Theory *IEEE Trans. Med. Imaging* **19** 261–70

[27] Qi J 2003 A unified noise analysis for iterative image estimation *Phys. Med. Biol.* **48** 3505–19

[28] Qi J and Leahy R M 2000 Resolution and noise properties of MAP reconstruction for fully 3D PET *IEEE Trans. Med. Imaging* **19** 493–506

[29] Soares E J, Glick S J and Hoppin J W 2005 Noise characterization of blockiterative reconstruction algorithms. II. Monte Carlo simulations *IEEE Trans. Med. Imaging* **24** 112–21

[30] Li Y 2011 Noise propagation for iterative penalized-likelihood image reconstruction based on Fisher information *Phys. Med. Biol.* **56** 1083–103

[31] I Llacer E, Veklerov K J, Coakley E J and Hoffman J 1993 Nunez, Statistical analysis of maximum likelihood estimator images of human brain FDG studies, *IEEE Trans. Med. Imaging MI* **12** 215–31

[32] Wilson D W, Benjamin M, Tsui W and Barret H H 1994 Noise properties of the EM algorithm: II. Monte Carlo simulations *Phys. Med. Biol.* **39** 847–71

[33] Bernert M *et al* 2021 X-point radiation, its control and an ELM suppressed radiating regime at the ASDEX Upgrade tokamak *Nucl. Fusion* **61** 024001

[34] Bernert M *et al* 2021 X-point radiation, its control and an ELM suppressed radiating regime at the ASDEX Upgrade tokamak *Nucl. Fusion* **61** 024001

[35] Ruiz M, Nieto J, Costa V, Craciunescu T, Peluso E, Vega J and Murari A 2022 Acceleration of an algorithm based on the maximum likelihood bolometric tomography for the determination of uncertainties in the radiation emission on JET using heterogeneous platforms *Appl. Sci.* **12** 6798

[36] Vega J, Murari A, Dormido-Canto S, Gelfusa M *et al* 2022 Disruption prediction with artificial intelligence techniques in tokamak plasmas *Nat. Phys.* **18** 741–50